Materials Today Bio 39 (2026) 103463

Contents lists available at ScienceDirect

Materials Today Bio

journal homepage: www.journals.elsevier.com/materials-today-bio

Janus porphyrin-stabilized phase-transition theranostics for multimodal imaging-guided synergistic cancer therapy

Pei He [a,1], Qiang Zhu [a,b,1], Ruoyun Lin [a], Xin Zhou [a,b,*], Yu Li [a,b,**], Zhong-Xing Jiang [a,b,***]

[a] State Key Laboratory of Magnetic Resonance Spectroscopy and Imaging, National Center for Magnetic Resonance in Wuhan, Wuhan Institute of Physics and Mathematics, Innovation Academy for Precision Measurement Science and Technology, Chinese Academy of Sciences, Wuhan, 430071, China
[b] University of Chinese Academy of Sciences, Beijing, 100049, China

ARTICLE INFO

Keywords:
Phase-transition liquids
Multimodal imaging
Synergistic therapy
Self-assemble
Tetraphenylporphyrins

ABSTRACT

Acoustic and optical droplet vaporization (ADV/ODV) enables localized energy conversion through nanoscale phase transitions, offering a mechanism to couple imaging enhancement with therapeutic activation. However, achieving controlled vaporization while integrating multimodal imaging and therapy remains challenging. Here, we developed low-boiling-point fluorocarbons (**FO1**-**FO4**) as phase-transition liquids and Janus porphyrin amphiphiles (**TP1** and **TP2**) as energy mediators, which co-assemble into core-shell nanodroplets (**TFNP**) that unify vaporization dynamics with multimodal theranostics. **TFNP** responds to optical or acoustic excitation by converting droplets into microbubbles, amplifying fluorescence, photoacoustic, and ultrasound signals, while simultaneously activating photodynamic and sonodynamic therapy. Structure-property optimization identified **TP2** as an effective interfacial energy mediator, fluorophore, sonosensitizer, and photosensitizer, and **FO1** as a newly developed phase-transition liquid with a single ^{19}F resonance, enabling sensitive ^{19}F magnetic resonance imaging (^{19}F MRI) and controllable vaporization. Compared with the commonly used perfluorohexane, **FO1** provides **TFNP** with unparalleled photoacoustic, ultrasound, and ^{19}F MRI performance. Upon ADV/ODV triggering, **TFNP** synchronizes multimodal imaging enhancement with reactive oxygen species generation and antivascular effects, enabling spatially confined and temporally guided therapy. *In vivo* ^{19}F MRI permitted quantitative tracking of **FO1** retention and revealed a theranostic window of less than 10 hours for ADV/ODV nanodroplets. These findings demonstrate that rational molecular and interfacial engineering can significantly improve phase-transition theranostic performance while highlighting the importance of imaging-guided temporal optimization.

1. Introduction

Accurate diagnosis and effective therapy are essential for improving cancer outcomes [1–3]. However, no single imaging or treatment modality can fully meet clinical demands [4,5]. Among emerging theranostic strategies, acoustic and optical droplet vaporization (ADV/ODV) has attracted increasing attention because it enables localized energy conversion through nanoscale liquid-gas phase transitions. Upon optical or acoustic stimulation, phase-transition nanodroplets can be transformed into resonant microbubbles, leading to signal amplification in ultrasound imaging (USI) and photoacoustic imaging (PAI) [6–9]. Moreover, *in situ* vaporization within tumors can induce vascular disruption, enhance membrane permeability, and promote therapeutic payload release [10–12]. These features make ADV/ODV-based nanodroplets promising platforms for imaging-guided cancer therapy. Nevertheless, their clinical translation remains hindered by challenges

* Corresponding author. State Key Laboratory of Magnetic Resonance Spectroscopy and Imaging, National Center for Magnetic Resonance in Wuhan, Wuhan Institute of Physics and Mathematics, Innovation Academy for Precision Measurement Science and Technology, Chinese Academy of Sciences, Wuhan, 430071, China.
** Corresponding author. University of Chinese Academy of Sciences, Beijing, 100049, China.
*** Corresponding author. University of Chinese Academy of Sciences, Beijing, 100049, China.
E-mail addresses: xinzhou@apm.ac.cn (X. Zhou), liyu@apm.ac.cn (Y. Li), zxjiang@apm.ac.cn (Z.-X. Jiang).
[1] These authors contribute equally to this work.

https://doi.org/10.1016/j.mtbio.2026.103463
Received 27 April 2026; Received in revised form 30 June 2026; Accepted 14 July 2026
Available online 14 July 2026

in balancing volatility, stability, activation threshold, and *in vivo* controllability.

To maximize the clinical utility of ADV/ODV nanodroplets, precise integration with multimodal imaging and therapy is required. Fluorine-19 magnetic resonance imaging (^{19}F MRI) provides quantitative "hot spot" images with negligible background signals, but suffers from intrinsically low sensitivity [13–15]. Fluorescence imaging (FLI) and PAI offer high sensitivity, yet their penetration depth is limited. USI enables real-time assessment but provides relatively low contrast [16–19]. Combining ^{19}F MRI, FLI, PAI, and USI can overcome the limitations of individual modalities and generate complementary structural, functional, and molecular information [20]. Such multimodal imaging is particularly valuable for monitoring nanodroplet accumulation, activation, and clearance, thereby enabling spatiotemporal guidance of therapy.

In parallel, the development of synergistic therapeutic strategies is essential for effective image-guided intervention. Photodynamic therapy (PDT) generates reactive oxygen species (ROS) upon light activation, providing high selectivity but limited penetration depth [21–23]. Sonodynamic therapy (SDT), driven by ultrasound, affords deeper tissue penetration and favorable safety profiles, although ROS yields are generally lower [24,25]. When combined, PDT and SDT can complement each other and achieve enhanced therapeutic efficacy [26]. However, successful implementation of multimodal imaging-guided combination therapy critically depends on multifunctional agents capable of mediating both diagnostic and therapeutic processes.

Tetraphenylporphyrins represent attractive candidates for this purpose because of their strong fluorescence emission and efficient ROS generation under optical and acoustic excitation [27,28]. Nevertheless, their poor water solubility, strong aggregation tendency, and aggregation-induced quenching (ACQ) severely compromise fluorescence intensity, ROS production, and formulation stability [29]. In addition, their limited tumor selectivity further restricts clinical translation. Although structural modification strategies have been explored to address these issues, such approaches are often complex and inefficient [30], highlighting the need for more practical and versatile design principles.

In addition to optimizing energy mediators, the physicochemical properties of phase-transition liquids play a decisive role in determining nanodroplet performance. Clinically relevant nanodroplets have primarily employed perfluorocarbons such as perfluorohexane, perfluoropentane, and their mixtures. However, these materials suffer from inherent trade-offs among volatility, stability, activation threshold, and imaging readout [31,32]. Despite containing multiple fluorine atoms, most conventional perfluorocarbons generate multiple ^{19}F nuclear magnetic resonance (NMR) peaks, resulting in low ^{19}F MRI sensitivity and chemical-shift artifacts. Furthermore, their high density and suboptimal phase-transition characteristics often impair nanodroplet stability and USI performance [33,34]. Consequently, there is an urgent need to develop novel phase-transition fluorocarbons that exhibit an intense singlet ^{19}F NMR peak and optimized physicochemical properties for controlled vaporization and quantitative tracking.

Herein, an "all-in-one" phase-transition nanodroplet system (**TFNP**) was developed for FLI/^{19}F MRI/PAI/USI-guided synergistic PDT/SDT/

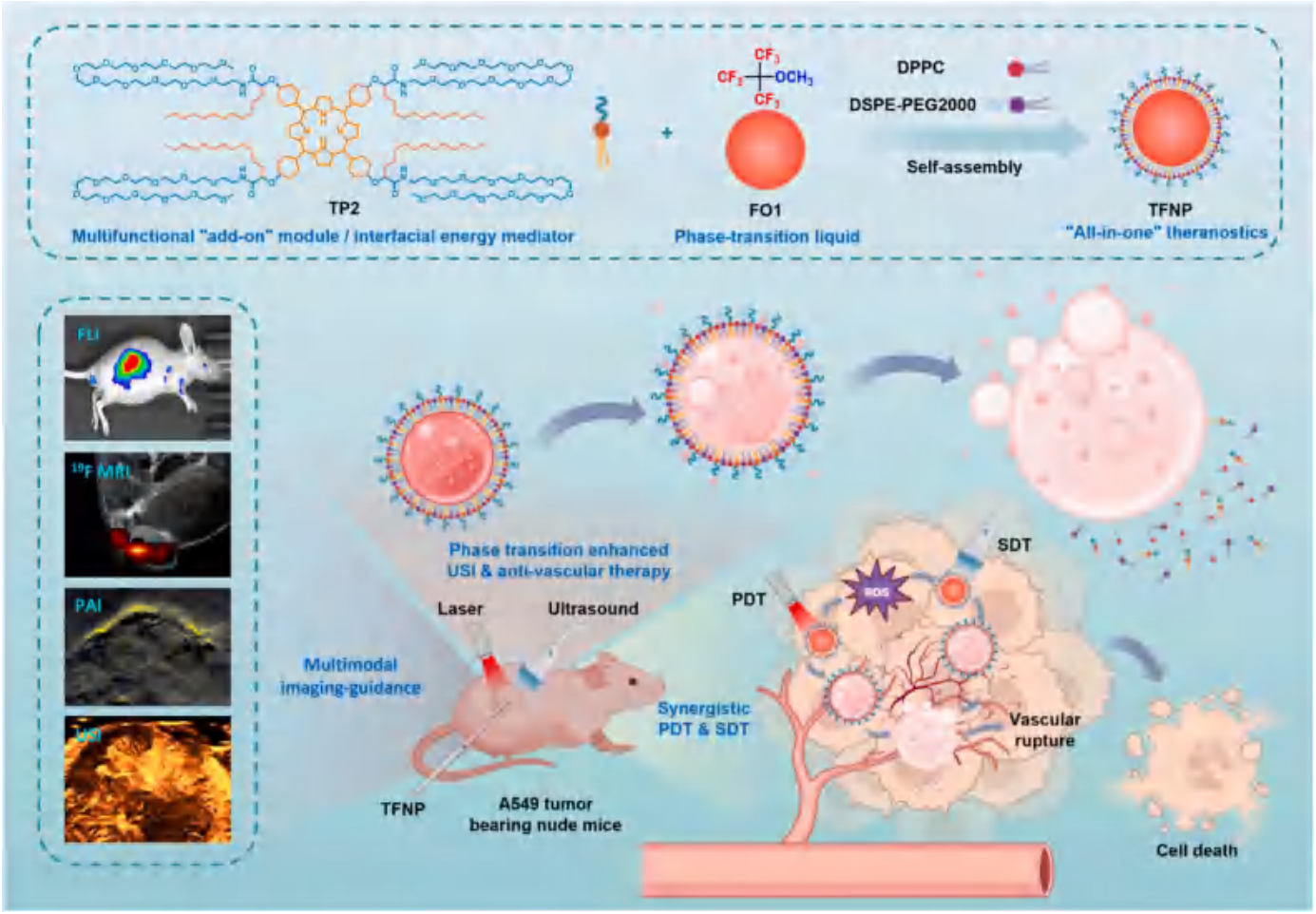

Scheme 1. Schematic illustration of "all-in-one" theranostic nanodroplet **TFNP** self-assembled from Janus amphiphilic tetraphenylporphyrin **TP2** and phase-transitional liquid **FO1** for FLI/^{19}F MRI/PAI/USI-guided synergistic PDT/SDT/anti-vascular therapy of lung cancer.

anti-vascular therapy of lung cancer through the self-assembly of Janus amphiphilic tetraphenylporphyrins (**TPs**) and phase-transition perfluoro-*tert*-butyl ethers (**FOs**) (Scheme 1). Octopus-shaped Janus **TPs** were symmetrically functionalized with four hydrophilic monodisperse undeca(ethylene glycol) chains and hydrophobic alkyl segments, enabling stable localization at the fluorocarbon-water interface. Within the nanodroplet architecture, **TPs** function as fluorophores with suppressed ACQ, photoacoustic contrast agents, photosensitizers, and sonosensitizers, while simultaneously acting as interfacial energy mediators that channel optical and acoustic energy into the fluorocarbon core. The **FO** core serves as both a phase-transition medium and a ^{19}F MRI reporter. It amplifies photoacoustic and ultrasound signals upon vaporization and delivers an intense singlet ^{19}F NMR signal from nine equivalent fluorine atoms, enabling sensitive and quantitative self-tracking. These complementary imaging modalities were integrated to provide spatiotemporal guidance throughout imaging-guided therapy. Specifically, FLI visualizes tumor accumulation, ^{19}F MRI quantitatively tracks the fluorocarbon core and determines the effective therapeutic window, whereas PAI and USI monitor phase-transition activation through photoacoustic enhancement and microbubble generation, respectively. By systematically tuning the alkyl chains of **TPs** (**TP1**: hexyl; **TP2**: dodecyl) and **FOs** (**FO1**: methyl; **FO2**: ethyl; **FO3**: propyl; **FO4**: butyl), structure-property relationships were established to identify optimal combinations. Both ^{19}F MRI and FLI were employed to monitor *in vivo* nanodroplet behavior and determine the therapeutic window, revealing a practical sub-10-h theranostic window with one-dose, multiple-imaging/therapy potential. Furthermore, multimodal imaging-guided PDT, SDT, and anti-vascular therapy using **TFNP** demonstrated pronounced synergistic efficacy following both intratumoral (*i.t.*) and intravenous (*i.v.*) administration, elucidating the central roles of **TP2** and **FO1** in therapeutic performance. Collectively, this study demonstrates that rational molecular and interfacial engineering of phase-transition liquids and multifunctional energy mediators can substantially enhance ADV/ODV-based theranostics. The **TFNP** platform provides a robust strategy for synchronizing multimodal imaging with temporally optimized synergistic therapy, thereby offering a promising framework for precision cancer theranostics.

2. Materials and methods

2.1. Materials

Unless otherwise noted, solvents and reagents were purchased from commercial suppliers and used as received. DSPE-PEG2000 was purchased from Adamas (Shanghai, China). The human lung adenocarcinoma cell line (A549) was purchased from Beyotime (Shanghai, China), Human normal lung epithelial cell line (BEAS-2B) was purchased from Xavier (Wuhan, China). The cells were cultured in Dulbecco's Modified Eagle's Medium (DMEM) supplemented with 10% fetal bovine serum (FBS) and 1% penicillin-streptomycin. Cells were incubated at 37 °C in a humidified 5% CO_2 atmosphere. CCK-8, DAPI, DCFH-DA and Calcein-AM/PI staining were purchased from Beyotime (Shanghai, China). SOSG was purchased from MeilunBio (Dalian, China). RIPA lysis buffer was purchased from Boerfu (Wuhan, China).

2.2. Animals

Female BALB/c nude mice of 5 weeks old were purchased from Beijing Vital River Laboratory Animal Technology Co., Ltd. (Beijing, China) and fed with SPF-grade mouse feed. All animal experiments were conducted in accordance with the Guidelines for Animal Care and Use and were approved by the Ethics Committee of the Innovation Academy for Precision Measurement Science and Technology, Chinese Academy of Sciences (APM24006A). A xenograft tumor model was established in nude mice (female, 20 ± 2 g, 5-6 weeks old) by injecting A549 cells (5×10^6 cells in 100 μL of PBS) into the right hind flank.

2.3. CMC of amphiphilic tetraphenylporphyrin *TPs*

The critical micelle concentration (CMC) was determined using the pyrene fluorescence probe method. A stock solution of pyrene in acetone was prepared and aliquoted into vials. Following evaporation of the solvent in the dark over 12 hours to deposit pyrene crystals, 1 mL of aqueous solutions of the compound at different concentrations in PBS (pH 7.4) was added. The fluorescence intensities of pyrene at 373 nm (I_{373}) and 384 nm (I_{384}) were recorded. The CMC value was determined from the breakpoint in the plot of the I_{373}/I_{384} ratio versus the logarithm of the surfactant concentration.

2.4. Determination of the singlet oxygen generation capacity (SOSG)

Singlet oxygen generation was evaluated using Singlet Oxygen Sensor Green (SOSG) as a fluorescent probe. An aqueous solution of **TP2** (5 μM in PBS) was mixed with an SOSG solution (5 μM in PBS) and irradiated with a 660 nm laser (0.5 W cm^{-2}). Fluorescence emission spectra were recorded at predetermined time intervals (λex = 504 nm), and the fluorescence intensity at 525 nm was used to evaluate the kinetics of singlet oxygen generation.

2.5. Formulation of nanodroplet

TFNP was prepared via a modified Ouzo method. Briefly, DPPC and DSPE-PEG2000 were dissolved in ethanol at a molar ratio of 20:1, yielding a total lipid concentration of 1.24 mg/mL. **TP2** (1 mg) and **FO1** (50 μL) were then added to 1 mL of the ethanolic lipid solution and dissolved completely. Subsequently, an aqueous phase composed of water, propylene glycol, and glycerol (7:2:1 v/v/v) was added. The resulting nanodroplets were collected by centrifugation, the supernatant was discarded, and the pellet was resuspended to remove residual ethanol and unincorporated lipids. This purification procedure was repeated three times. Finally, the purified **TFNP** was resuspended in water and adjusted to a final volume of 1 mL, yielding a formulation containing 100 μM **TP2** and 550 mM ^{19}F, as determined by internal standard quantification.

2.6. Quantitative ^{19}F NMR and ^{19}F MRI of nanodroplets

A 100 μL aliquot of **TFNP** was mixed with a deuterium oxide (D_2O) solution of sodium trifluoromethanesulfonate as the internal standard, giving a final ^{19}F concentration of 30 mM for the standard. The mixture was then diluted with PBS to a final volume of 500 μL. ^{19}F NMR spectra were acquired on a 500 MHz NMR spectrometer.

TFNP and **PFHNP** were diluted with PBS to give ^{19}F concentrations of 110, 55, 27.5, 13.8, and 6.9 mM, respectively. Each sample (2 mL) was transferred into an MRI tube and imaged on a 400 MHz Bruker BioSpec MRI scanner with a scan time of 256 seconds. The relationship between the logarithm of ^{19}F signal intensity (SI) and the logarithm of ^{19}F concentration was analyzed. Imaging parameters were: number of averages = 64, matrix size = 32 × 32, RARE factor = 4, TR = 1000.0 ms, TE = 3.0 ms.

2.7. Hemolysis assay

Whole blood (0.5 mL) collected from BALB/c nude mice was mixed with 1 mL PBS and centrifuged at 4500 rpm for 5 min to isolate red blood cells (RBCs). The RBCs were then washed five times with PBS. A 2% erythrocyte suspension was then mixed with an equal volume of water, PBS, **TFNP**/**PFHNP** solutions at **TP2** concentrations of 0.5, 1, 5, 10, 20, 40, 60 and 80 μM, respectively. The mixtures were incubated at room temperature for 3 h, followed by centrifugation at 4500 rpm for 3 min. Hemolysis was assessed by measuring the absorbance of the supernatant at 541 nm, using water-treated and PBS-treated erythrocytes as positive and negative controls, respectively.

2.8. Cellular uptake of *TFNP*

A549 cells were seeded into 20 mm confocal dishes at a density of 2 × 10^5 cells per dish. After 24 hours of incubation, the DMEM medium was removed. Fresh medium containing **TFNP** (10 μM **TP2**) was added and incubated for 1, 3, 6, 12 and 24 hours, respectively. Subsequently, the culture medium was carefully discarded, and the cells were washed with PBS (pH 7.4). The cells were then fixed with 4% paraformaldehyde for 15 minutes, followed by three washes with PBS. Next, the cells were stained with 200 μL DAPI for 10 minutes and washed six times with PBS. The cellular uptake of **TFNP** was observed by confocal laser scanning microscopy (CLSM).

2.9. Detection of ROS in vitro and live/dead cell staining assays

A549 cells were seeded onto 35 mm confocal dishes at a density of 1 × 10^5 cells and incubated with **TFNP** (**TP2** = 10 μM) for 12 h at 37 °C and 5% CO_2. After washing once with PBS, the cells were incubated with DCFH-DA (25 μM) for 30 min. The cells were then washed again with PBS and followed by exposure to a 660 nm laser (0.5 W cm^{-2}, 5 min) and/or ultrasound (1 MHz, 1 W cm^{-2}, 5 min). Then, the cells were fixed with 4% paraformaldehyde for 10 min and replaced with 1 mL PBS. Finally, confocal fluorescence imaging was performed. Cells treated with PBS instead of **TFNP** were used as the control.

A549 cells were seeded onto 35 mm confocal dishes at a density of 1 × 10^5 cells and incubated with **TFNP** (**TP2** = 10 μM) for 6 h. Following exposure to a 660 nm laser (0.5 W cm^{-2}, 5 min) and/or ultrasound (1 MHz, 1 W cm^{-2}, 5 min), the cells were further cultured for 6 h and stained with calcein-AM and PI for 30 min. Finally, confocal fluorescence imaging was performed. PBS + laser and PBS + ultrasound were used as irradiation controls.

2.10. Acute toxicity experiments

Before the *in vivo* experiments, BALB/c nude mice were used for acute toxicity tests. **TFNP** (**TP2**: 5 mg/kg) was administered via tail vein injection, and the mice were monitored for general health and body weight following administration. After receiving three consecutive intravenous injections of **TFNP** every other day, no abnormalities or weight loss were observed for 7 days. After the experiment, no abnormalities in tissues or organs were found during the anatomical observation of the mice.

2.11. In vivo FLI, ^{19}F MRI, PAI and USI

FLI: When the tumor size reached approximately 200~300 mm^3, mice bearing A549 tumors were *i. v.* injected with 100 μL of **TFNP** (**TP2**: 5.0 mg/kg). Biodistribution of **TFNP** was monitored by fluorescence imaging at 12, 24, 36, 48, 72 and 96 hours post-injection (n = 3). During image acquisition, mice were anesthetized with 2% isoflurane and imaged using an IVIS imaging system (430 nm excitation, 680 nm emission).

^{19}F MRI: The mice had free access to water and food until tumor size reached about 200 mm^3. Mice bearing A549 tumors received *i. t.* injection with 20 μL of **TFNP** (**TP2**: 1.0 mg/kg) (n = 3). $^{1}H/^{19}F$ MRI was performed on a 400 MHz MRI system. ^{1}H MRI: RARE sequence (TR = 4000 ms, TE = 11 ms, FOV = 30 mm × 30 mm, slice thickness = 1 mm, RARE factor = 8, matrix size = 256 × 256). ^{19}F MRI: RARE sequence (TR = 1000 ms, TE = 3 ms, FOV = 37 mm × 37 mm, slice thickness = 30 mm, matrix size = 32 × 32, 64 averages, scan time = 8 min 32 s).

PAI: Mice bearing A549 tumors received *i. t.* injection with 20 μL of **TFNP** (**TP2**: 1.0 mg/kg) (n = 3). Tumor PA intensity was measured at 0, 0.5, 3, and 5 hours post-injection. PAI was performed using an MSOT inVision system equipped with a 40 MHz, 256-element linear array transducer on tumors. A 680-nm excitation filter was used.

USI: Mice bearing A549 tumors (n = 3) received *i. t.* injection with 20 μL of **TFNP** (**TP2**: 1.0 mg/kg). Tumor B-Mode and CEUS intensity were measured at 0, 0.5, 3, and 5 hours post-injection. USI was performed using a color Doppler ultrasound system equipped with a 15-30 MHz transducer over the target tumor area. The B/M knob was rotated to adjust gain and imaging depth, and to optimize the transducer frequency.

2.12. In vivo tumor inhibition

Intratumoral model: When the tumor volume reached about 150 mm^3, the mice bearing A549 tumors were randomly assigned to five groups: (1) saline, (2) **TFNP**, (3) **TFNP** + laser, (4) **TFNP** + ultrasound, (5) **TFNP** + ultrasound + laser, with 5 mice in each group. The mice in group 1 were intratumorally injected with saline, the mice in groups 2-5 were intratumorally injected with **TFNP** solution (**TP2**: 1 mg/kg). On days 0, 2, 4 and 6, the mice in each group received injections of 20 μL of nanodroplets. 0.5 hours after administration, groups 3 and 5 underwent irradiation with a 660 nm laser (0.5 W cm^{-2}, 5 min), groups 4 and 5 underwent irradiation with an ultrasound device (1 MHz, 1 W cm^{-2}, 5 min). The weight and tumor volume of the nude mice were measured and recorded every two days. After 16 days of treatment, the mice were sacrificed, and the major organs and tumors were collected, fixed with 4% paraformaldehyde, embedded in paraffin, and sectioned for H&E, Ki-67, TUNEL and CD31+**TP2** staining.

Intravenous model: When the tumor volume reached about 150 mm^3, the mice bearing A549 tumors were randomly assigned to six groups: (1) saline, (2) saline + ultrasound + laser, (3) **TFNP**, (4) **TFNP** + laser, (5) **TFNP** + ultrasound, (6) **TFNP** + ultrasound + laser, with 5 mice in each group. The mice in groups 1-2 were intravenously injected with saline, the mice in groups 3-6 were intravenously injected with **TFNP** solution (**TP2**: 5 mg/kg). On days 0, 4, 8 and 12, the mice in each group received injections of 100 μL of nanodroplets. 36 hours after administration, groups 2, 4 and 6 underwent irradiation with a 660 nm laser (0.5 W cm^{-2}, 5 min), groups 2, 5 and 6 underwent irradiation with an ultrasound device (1 MHz, 1 W cm^{-2}, 5 min). The weight and tumor volume of the nude mice were measured and recorded every two days. After 14 days of treatment, the mice were sacrificed, and the major organs and tumors were collected, fixed with 4% paraformaldehyde, embedded in paraffin, and sectioned for H&E, Ki-67, TUNEL and CD31+**TP2** staining.

2.13. Statistical analysis

The analyzed data are presented as mean ± standard deviation of n ≥ 3 replicates unless otherwise stated. Statistical significance was assessed by unpaired *t*-test. Asterisks indicate significant differences: $p < 0.05$ was considered the probability threshold for statistical significance, $^{*}p < 0.05$, $^{**}p < 0.01$, $^{***}p < 0.001$.

3. Results and discussion

3.1. Synthesis and characterization of *TPs* and *FOs*

TPs were synthesized in just three steps from readily available reagents on gram scales with high overall yields >46% (Fig. S1a). Briefly, tetraphenylporphyrin **1** was alkylated with either methyl 2-bromooctanoate **2** or methyl 2-bromotetradecanoate **3** in the presence of K_2CO_3 to give tetra-esters **4** and **5**, respectively. Hydrolysis of the esters afforded tetra-acids **6** and **7**, which were then coupled to monodisperse α-amino-ω-methyl undeca(ethylene glycol) to yield **TP1** and **TP2**, respectively. Meanwhile, **FO**s were prepared on multigram scales via a single-step Williamson ether synthesis using potassium perfluoro-*tert*-butoxide and alkyl halides **8**-**11** (Fig. S1b). After fractional distillation, only the fraction corresponding to the boiling point of the target **FO** was collected. **TP**s and **FO**s were characterized by $^{1}H/^{13}C/^{19}F$ NMR and mass

spectrometry (Supporting Information).

TPs were water-soluble due to their four hydrophilic undeca (ethylene glycol), exhibiting the characteristic ultraviolet-visible (UV-Vis) absorption and FL emission of tetraphenylporphyrins in phosphate-buffered saline (PBS, Fig. 1a). When switching the solvent from methanol to water, **TP1** showed a sharp decrease and red shift in UV-Vis absorption around 40% water, while **TP2** exhibited similar changes only around 20% water (Fig. 1b). Meanwhile, **TP1** exhibited increasing FL emission followed by decreasing FL emission, while **TP2** solely exhibited decreasing FL emission (Fig. 1c). Furthermore, **TP1** displayed increasing emission at lower concentrations and decreasing emission at higher concentrations, whereas **TP2** exhibited only decreasing emission (Fig. S2). Critical micelle concentration (CMC) measurements showed **TP2** has a significantly lower CMC than **TP1** (1.2 μM versus 5.6 μM, Fig. 1d). Compared to the poor solubility and severe ACQ of tetraphenylporphyrins [35], **TP**s exhibited high solubility and distinct FL emission in water. The lower CMC and the sharper decrease in absorption and emission in the presence of water for **TP2** than for **TP1** suggest that the more hydrophobic dodecyl groups promote aggregation in water.

The phototherapy potential of **TP**s was assessed using SOSG. **TP2** produced more singlet oxygen ($^1O_2$) than **TP1** (Fig. 1e). The $^1O_2$ quantum yields (Φ_Δ) in chloroform were measured using diphenylbenzopyran (DPBF) with tetraphenylporphyrin **1** as the reference ($\Phi_\Delta = 0.5$) [36], revealing higher Φ_Δ values for **TP2** ($\Phi_\Delta = 0.7$) than for **TP1** ($\Phi_\Delta = 0.6$). Although the temperature increase was less than 5 °C, **TP2** exhibited a higher photothermal effect than **TP1** (Fig. 1f). Cytotoxicity was evaluated using a Cell Counting Kit-8 (CCK-8) assay in normal lung epithelial BEAS-2B cells and lung cancer A549 cells. In BEAS-2B cells, **TP**s maintained >80% viability up to 32 μM, while **TP1** became cytotoxic above this level (Fig. 1g). In A549 cells, **TP**s were cytotoxic, with **TP1** exhibiting much higher cytotoxicity than **TP2** (Fig. 1h). These results are consistent with a previous study of "octopus-shaped" amphiphiles showing that shorter alkyl chains preferentially interact with cell membranes, particularly in cancer cells, thereby enhancing cytotoxicity [37]. The comparative study indicates that the longer alkyl chains in **TP**s promote $^1O_2$ generation and biocompatibility. Thus, **TP2** was selected for further study.

Finally, the physicochemical properties of **FO**s were investigated. An increase in alkyl chain length was associated with a decrease in density and an increase in boiling point (Fig. 1i). **FO**s produced an intense singlet ^{19}F NMR peak around -73.50 ppm, enabling sensitive ^{19}F MRI with a high signal-to-noise ratio (SNR) >18 at 0.5 mM in 256 seconds (Fig. 1i). Among them, **FO1** has an optimal boiling point for phase-transition application [38]. For comparison, **PFH** has the same boiling point but a much higher density, which promotes nanodroplet settling in physiological conditions and reduces nanodroplet stability [39,40]. Furthermore, **PFH** produces multiple ^{19}F NMR peaks, while only one of them can be used for ^{19}F MRI, resulting in significantly lower ^{19}F MRI sensitivity (SNR = 5.4). Therefore, **FO1** was identified as possessing optimal boiling points, moderate density, and a sensitive ^{19}F MRI signature for intrinsic self-tracking.

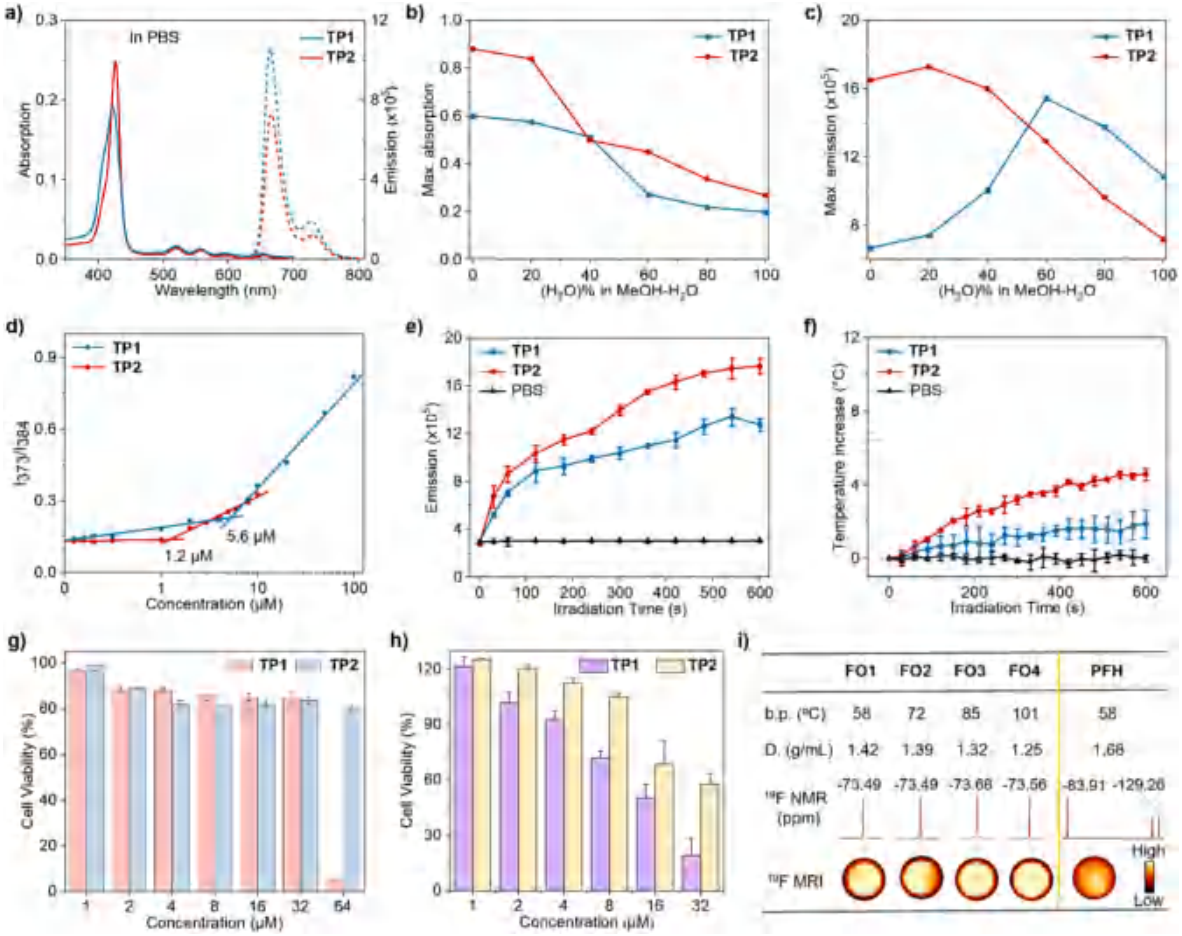

Fig. 1. UV-Vis and FL spectra of 10 μM **TP** in PBS (a). Maximum UV-Vis absorption (b) and FL emission (c) of 10 μM **TP** in a MeOH-H_2O system. CMC measurement using the FL of pyrene (d), $^1O_2$ generation detected by the FL of SOSG (e, 5 μM), photothermal effect (f, 10 μM), and cytotoxicity in BEAS-2B cells (g) and A549 cells (h) of **TP**s. Boiling point (b.p.), density (D.), partial ^{19}F NMR spectra, and ^{19}F MRI images of **FO**s and **PFH** (i). 660 nm laser irradiation at 0.5 W cm^{-2} for 10 minutes was used in e and f.

3.2. Formulation and characterization of *TFNP*

The Ouzo method [41,42] was used to self-assemble **TP2** and **FO1** with phospholipids DPPC and DSPE-PEG2000, yielding a monodisperse nanodroplet (**TFNP**). Dynamic light scattering (DLS) revealed a mean diameter of 135 nm, a small polydispersity index (PDI) of 0.074, and a zeta potential of -24.6 mV (Fig. 2a). Transmission electron microscopy (TEM) confirmed its spherical morphology. **TFNP** remained stable for at least seven days at both 4 °C and 37 °C, as evidenced by negligible changes in particle size and PDI (Fig. 2b and Fig. S3a and b). Meanwhile, ^{19}F NMR measurements showed a gradual decrease in the ^{19}F signal over the same period, confirming the gradual volatilization of **FO1** (Fig. S3c–e). These results suggest that gradual **FO1** volatilization occurred without causing appreciable disruption of the nanodroplet

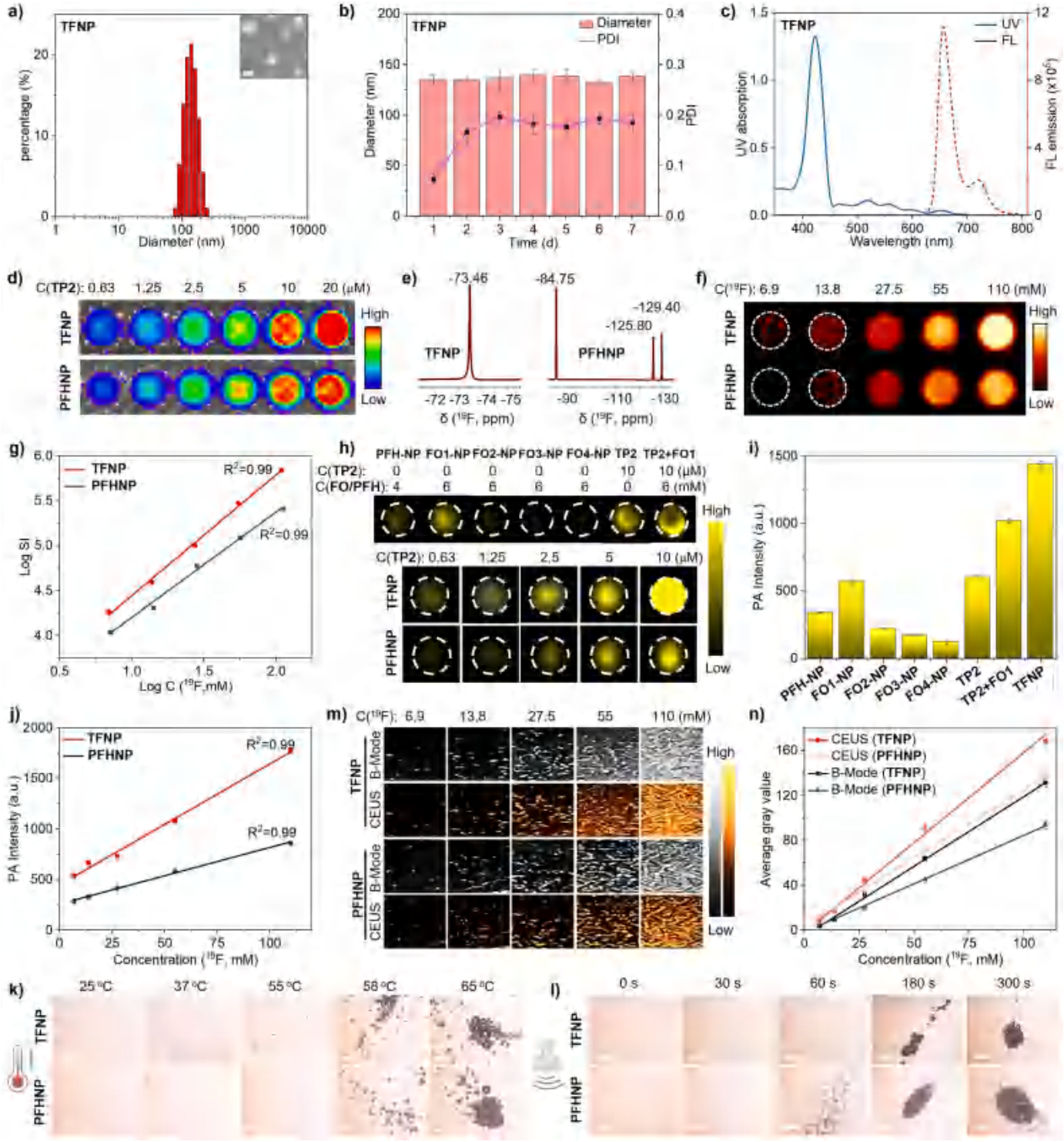

Fig. 2. DLS with inserted TEM image (a), particle size and PDI over 7 days (b), and UV-Vis and FL spectra (c) of **TFNP**. FLI (d), partial ^{19}F NMR spectra (e), ^{19}F MRI (f) and the corresponding plot of Log SI versus Log C(^{19}F) (g), PAI of a series of formulations and concentrations (h) and the corresponding SI (i) and plot of SI versus C(^{19}F) concentrations (j), microscope images under heating (k) and ultrasound exposure (l), USI (m) and the corresponding plot of gray value versus C(^{19}F) (n) of **TFNP** and **PFHNP**. Scale bar: 100 nm for a; 100 μm for k/l.

structure. For comparison, **TP2** and **PFH** were also formulated into a nanodroplet (**PFHNP**), which had a larger diameter of 182 nm and a small PDI of 0.073, yet remained stable at 4 °C (Fig. S4).

The multimodal imaging capability of **TFNP** and **PFHNP** was then compared. Excitation of the characteristic Q bands of tetraphenylporphyrin in **TFNP** and **PFHNP** at 423 nm resulted in strong FL emission at 658 nm (Fig. 2c and S5). Quantitative fluorescence quantum yield (QY) measurements in aqueous solution further showed that both **TP2** and

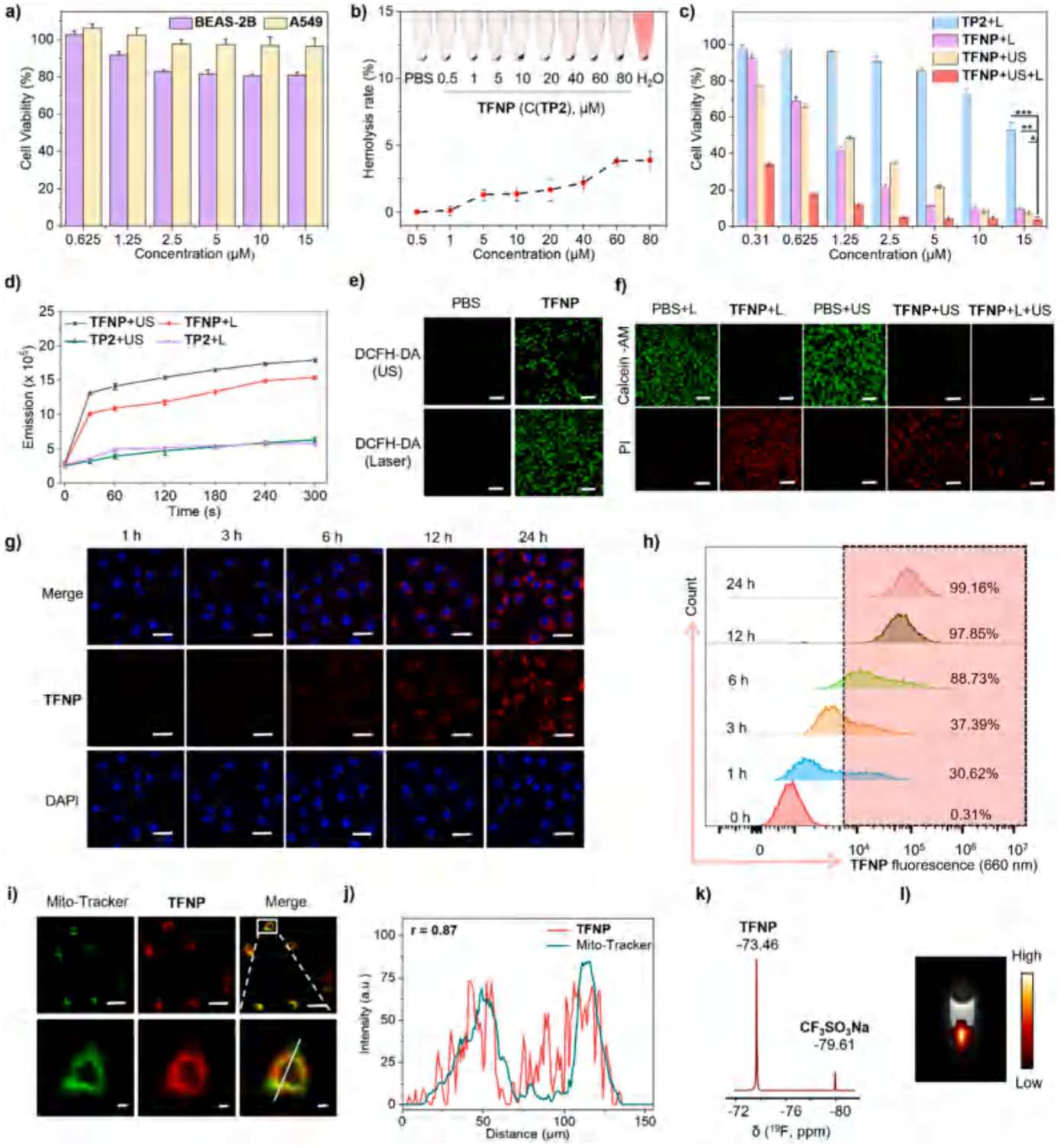

Fig. 3. CCK-8 assay in BEAS-2B and A549 cells (a) and hemolysis assay (b) of **TFNP**. CCK-8 assay in A549 cells treated with **TP2** or **TFNP** under laser (L)/ultrasound (US) irradiation (c). Time-dependent $^1O_2$ generation of **TP2** and **TFNP** under irradiation, detected by SOSG (d, 1 μM **TP2**). Confocal images of A549 cells with DCFH-DA staining (e) and calcein-AM/propidium iodide double staining (f) after the indicated treatments. Time-dependent confocal images (g, scale bar: 100 μm) and flow cytometry (h) of **TFNP**-treated A549 cells. Colocalization images of Mito-tracker and **TFNP**-treated A549 cells (i, scale bar: 100 μm for upper, 25 μm for lower) and FL intensity correlation plot along the white lines in the confocal images (j). Partial ^{19}F NMR spectrum (k) and $^1H/^{19}F$ MRI image (l) of **TFNP**-treated A549 cells. 5 minutes of 660 nm laser irradiation at 0.5 W cm^{-2} was used in all cases. Data are presented as mean ± SD; $^*p < 0.05$, $^{**}p < 0.01$, $^{***}p < 0.001$, n = 3.

TFNP exhibited higher QYs than **TPP-NP** (Table S1), where **TPP-NP** is a control nanodroplet of tetraphenylporphyrin (TPP) prepared under identical formulation conditions. Concentration-dependent FLI in a 96-well plate revealed their comparable FLI capabilities (Fig. 2d). **TFNP** produced an intense singlet ^{19}F NMR peak (Fig. 2e) with T_1 of 2.008 seconds and T_2 of 1.382 seconds. The 100% ^{19}F utility and the high T_2/T_1 ratio of 0.69 facilitated its sensitive ^{19}F MRI at a low ^{19}F concentration of 6.9 mM with an SNR of 2.99 in 256 seconds (Fig. 2f). In contrast, **PFHNP** produced three ^{19}F NMR peaks and exhibited up to 3.21-fold lower SNR. Furthermore, the logarithm of ^{19}F MRI signal intensity (SI) of **TFNP** and **PFHNP** scaled linearly with the logarithm of ^{19}F concentration (Fig. 2g), supporting quantitative imaging and accurate concentration readouts.

The photoacoustic imaging (PAI) performance of phase-transition liquids (**FOs** and **PFH**) was evaluated using corresponding nanodroplets (**FO-NPs** and **PFH-NP**), prepared analogously to **TFNP** but omitting **TP2**. Under 680 nm laser irradiation at an equal ^{19}F concentration, the photoacoustic intensity of **FO-NPs** diminished with increasing boiling point of **FO** (Fig. 2h and i), with **FO1-NP** yielding the highest signal. Although **FO1** and **PFH** share the same boiling point, **FO1-NP** generated a 40% stronger photoacoustic signal than **PFH-NP**. A physical mixture of **TP2** and **FO1** also exhibited an enhanced PA signal compared with **FO1-NP** or **TP2** alone, whereas **TFNP** generated an even stronger PA signal than the physical mixture, suggesting a synergistic enhancement beyond simple physical superposition. Concentration-dependent studies showed a linear increase in photoacoustic intensity with rising **TP2** concentration for both **TFNP** and **PFH-NP**, with **TFNP** consistently outperforming the latter (Fig. 2j).

The phase-transition behaviors of **TFNP** and **PFHNP** were evaluated using optical microscopy. Upon heating or ultrasound exposure, **TFNP** generated larger gas bubbles, whereas **PFHNP** formed clusters of smaller, sporadic microbubbles, even under mild conditions (37 °C or 30 seconds of ultrasound), indicating premature and less controllable vaporization (Fig. 2k and l). Notably, **TFNP** remained stable until exposed to sufficient thermal (58 °C) or acoustic energy (180 seconds of ultrasound), demonstrating superior spatiotemporal control. Replacing **FO1** in **TFNP** with **FO2** resulted in nanodroplets that showed significantly fewer bubbles upon ultrasound or laser exposure, consistent with **FO2**′s higher boiling point (Fig. S6). When exposed repeatedly to a laser every 5 minutes, both **TFNP** and **PFHNP** generated consistent gas bubbles for up to three cycles, with significantly fewer bubbles observed afterward (Fig. S7). Similarly, steady gas bubbles were observed after two and three cycles of ultrasound or heating, respectively. These results indicate that both nanodroplets can undergo multiple, reproducible phase-transition cycles, demonstrating a one-dose, multi-phase-transition capability. The gas bubbles produced by **TFNP** and **PFHNP** generated a strong contrast in B-mode ultrasound and contrast-enhanced ultrasound (CEUS) (Fig. 2m), with signal intensity increasing linearly with ^{19}F concentration (Fig. 2n). Overall, **TFNP** exhibited significantly higher USI sensitivity and stability than **PFHNP**.

3.3. *In vitro biocompatibility and synergistic therapy of **TFNP***

Next, the *in vitro* therapeutic potential of **TFNP** was investigated. CCK-8 assays revealed >80% cell viability up to 15 μM **TP2** in both BEAS-2B and A549 cells (Fig. 3a). Hemolysis was less than 5% up to 80 μM **TP2**, confirming its high biocompatibility (Fig. 3b). In contrast, **PFHNP** exhibited poor biocompatibility with much lower cell viability and much higher hemolysis (Fig. S8). At 10 μM **TP2**, the **TP2** solution exhibited >70% cell viability after laser exposure, whereas **TFNP** exhibited <10% cell viability (Fig. 3c), suggesting a synergistic effect of **FO1** and **TP2**. Furthermore, the viability of **TFNP**-treated cells exposed to ultrasound was comparable to that of laser-exposed cells. Sequential laser and ultrasound exposure resulted in the lowest cell viability. The IC_{50} values of **TFNP** + laser, **TFNP** + ultrasound, and **TFNP** + laser + ultrasound were 1.82, 1.73, and 0.19 μM, respectively, corresponding to a calculated combination index (CI) of 0.224 (CI < 1), which indicates a strong synergistic therapeutic interaction. For comparison, **PFHNP** exhibited much lower PDT and SDT efficacy than **TFNP** (Fig. S9). These results demonstrate **TFNP**'s superior biocompatibility and therapeutic potential over **PFHNP**.

TP2 alone generated intracellular ROS under both laser and ultrasound irradiation (Fig. S10), confirming its dual photodynamic and sonodynamic activities at the cellular level. Compared with **TP2**, **TFNP** produced substantially more $^1O_2$ when exposed to laser or ultrasound (Fig. 3d), probably due to the enriched oxygen from **FO1**. DCFH-DA staining revealed strong green FL in **TFNP**-treated A549 cells upon ultrasound exposure and even stronger FL upon laser exposure (Fig. 3e), suggesting robust ROS generation in the cells. Calcein-AM/propidium iodide double staining showed intense green FL of live cells in PBS-treated cells and strong red FL of dead cells in **TFNP**-treated A549 cells under different irradiation conditions (Fig. 3f), with the combined laser and ultrasound treatment exhibiting the fewest viable cells. Notably, ultrasound exposure, particularly when combined with laser irradiation, likely caused partial detachment of severely damaged cells during the staining procedure, resulting in a lower apparent cell density in the representative fluorescence images. The enhanced therapeutic efficacy under combined treatment may arise from the complementary activation of **TP2** by laser and ultrasound through two distinct energy modalities, thereby allowing more effective therapeutic utilization of **TP2** than either treatment alone. Nevertheless, the detailed mechanism underlying this synergistic effect requires further investigation.

Confocal microscopy and flow cytometry of **TFNP**-treated A549 cells revealed maximum cellular uptake around 12 hours (Fig. 3g and h, and S11). Co-staining with Mito-Tracker revealed strong colocalization of **TP2** with mitochondria (Pearson's correlation coefficient, r = 0.87) (Fig. 3i and j), positioning it near a key organelle for ROS-mediated damage and favoring both PDT and SDT. This observation is consistent with previous observations reported for porphyrin-based photosensitizers [43], although the detailed mechanism remains to be elucidated. **TFNP**-treated A549 cell lysate displayed a distinct ^{19}F NMR peak at -73.46 ppm (Fig. 3k). Using sodium trifluoromethanesulfonate as an internal standard, the uptake was quantified as $\sim 3.47 \times 10^{12}$ ^{19}F per cell. Due to the high uptake level, the cells produced a “hot spot” ^{19}F MRI with an SNR of 4.65 in 256 seconds (Fig. 3l).

Collectively, these results established **TFNP** as a stable, monodisperse, multifunctional nanodroplet that can be conveniently prepared from **TP2** and **FO1**. **TFNP** combines favorable biocompatibility, efficient cellular uptake, robust ROS generation and PDT/SDT activity, supporting its subsequent *in vivo* evaluation.

3.4. *In vivo biocompatibility, biodistribution and multimodal imaging of **TFNP***

Acute toxicity of **TFNP** was first assessed in BALB/c nude mice, with no abnormalities or body weight loss observed after three consecutive *i. v.* injections (5 mg/kg **TP2**). To further evaluate long-term biosafety, BALB/c mice received four intravenous injections of **TFNP** (5 mg/kg) or saline over 16 days. No significant abnormalities were observed in body weight, hematological and serum biochemical parameters, or H&E staining of the major organs (Fig. S12), indicating favorable long-term biosafety.

Whole-body multimodal imaging was then performed on three BALB/c nude mice bearing an A549 xenograft tumor. After *i. v.* injection of **TFNP**, FL signals increased over time in the tumor, liver, and spleen, with high signal in the tumor region (Fig. 4a). Tumor FL signals peaked at 36 hours and remained high through 96 hours (Fig. 4b). *Ex vivo* FLI of internal organs and tumor at 36 hours confirmed strong FL signals in the tumor and liver (Fig. 4c and d), supporting effective tumor accumulation. Persistent tumor fluorescence was still observed at 5 and 7 days after *i. v.* injection, whereas only weak liver signals remained (Fig. S13),

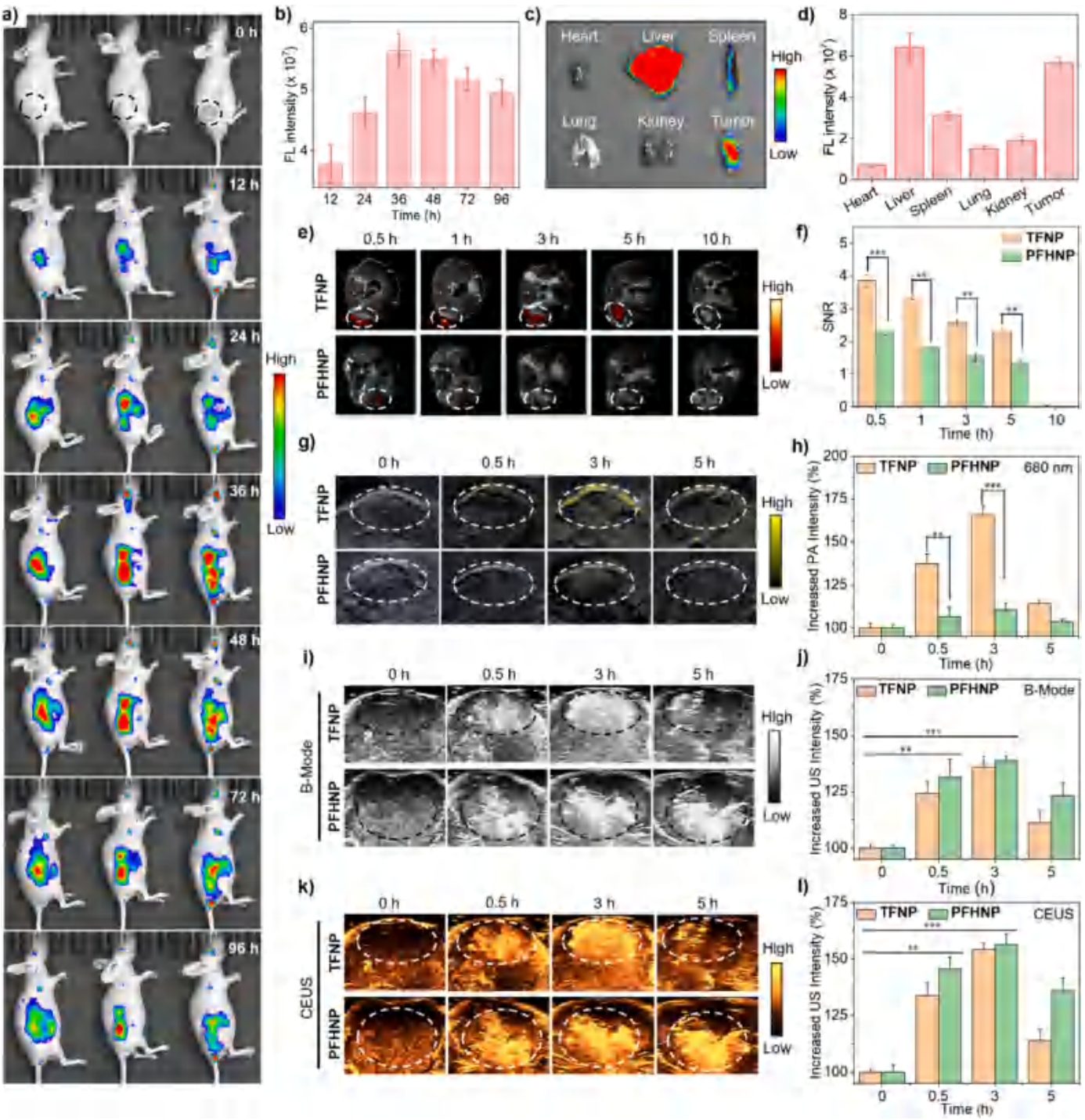

Fig. 4. Time-dependent FLI of BALB/c mice bearing A549 xenograft tumor after *i. v.* injection of **TFNP** (a) with corresponding intensity in tumor region (b). *Ex vivo* FL images (c) with corresponding intensity (f) of excised internal organs and tumor collected at 36 hours. Time-dependent ^{19}F MRI (e) with corresponding intensity (f), PAI (g) with corresponding intensity (h), USI (i, k) with corresponding gray value (j, l) after *i. t.* injection of **TFNP** and **PFHNP**. Dose: 1 mg/kg **TP2**.

indicating prolonged tumor retention accompanied by gradual hepatic clearance. Furthermore, after *i. t.* injections, **TFNP** produced a significantly stronger ^{19}F MRI signal than **PFHNP** (Fig. 4e and f), demonstrating **TFNP**'s high *in vivo* ^{19}F MRI sensitivity. However, the ^{19}F MRI signal declined rapidly over time and became negligible within 10 hours, whereas FL persisted beyond 96 hours. Mass spectrometric analysis further revealed a marked reduction in the **FO1** signal at 10 h after intratumoral injection (Fig. S14), directly confirming the loss of **FO1** following phase transition and gas escape. In contrast, the persistent fluorescence signal indicates that **TP2** remained retained within the tumor, consistent with its efficient cellular uptake and intracellular retention (Fig. 3). These results highlight that the therapeutic window of phase-transition nanodroplets is determined by the retention of the volatile fluorocarbon rather than by nanodroplet accumulation alone. Although phase-transition nanodroplets have been widely investigated, several previous studies selected treatment time points primarily based on nanodroplet accumulation [44], while the *in vivo* retention of the fluorocarbon core was rarely monitored directly. The ^{19}F MRI self-tracking ability of **FO1**/**PFH** reveals a critical but often overlooked constraint for phase-transition nanodroplets: their phase-transition

imaging and therapeutic activation windows are limited to within ~10 hours after administration, ideally within 5 hours. Failure to consider this time window may result in misinterpreting imaging or therapeutic outcomes.

The volatility at physiological temperature of **FO1** precluded reliable ^{19}F MRI tracking of systemically administered **TFNP**, as most of the agent escaped prior to reaching the tumor. However, substituting the low-boiling **FO1** with the higher-boiling **FO2** within the **TFNP** architecture enabled detectable ^{19}F MRI signals corresponding to tumor accumulation following *i. v.* injection (Fig. S15). This substitution highlights a principal advantage of **FO**s: their tunable physicochemical properties, which surpass those of conventional perfluorohexane. Furthermore, it establishes a strategy for calibrating the biodistribution of phase-transition nanodroplets through sensitive ^{19}F MRI.

Within the window, the PAI and USI capabilities of **TFNP** and **PFHNP** were compared. In **TFNP**-treated mice, tumor PA intensity increased after injection, peaking at 3 hours and then significantly decreasing at 5 hours. In contrast, **PFHNP** yielded a significantly lower PA intensity with minimal increase (Fig. 4g and h). These observations confirmed the synergistic effect of **FO1** and **TP2** in PAI (Fig. 2h and i). Similarly, USI showed maximal gray values in the tumor at 3 hours for both the **TFNP**- and **PFHNP**-treated mice in B-mode and CEUS (Fig. 4i-l). The gradually decreasing PAI and USI signals 3 hours post-administration confirmed the escape of **FO1** and **PFH** from the mice. Overall, **TFNP** provided significantly higher ^{19}F MRI and PAI performance than **PFHNP**, and comparable FLI and USI performance for multimodal tumor imaging.

The *in vivo* fates of **FO1** and **TP2** were monitored via ^{19}F MRI and FLI. Following *i. t.* injection, laser, ultrasound, or combined laser/ultrasound

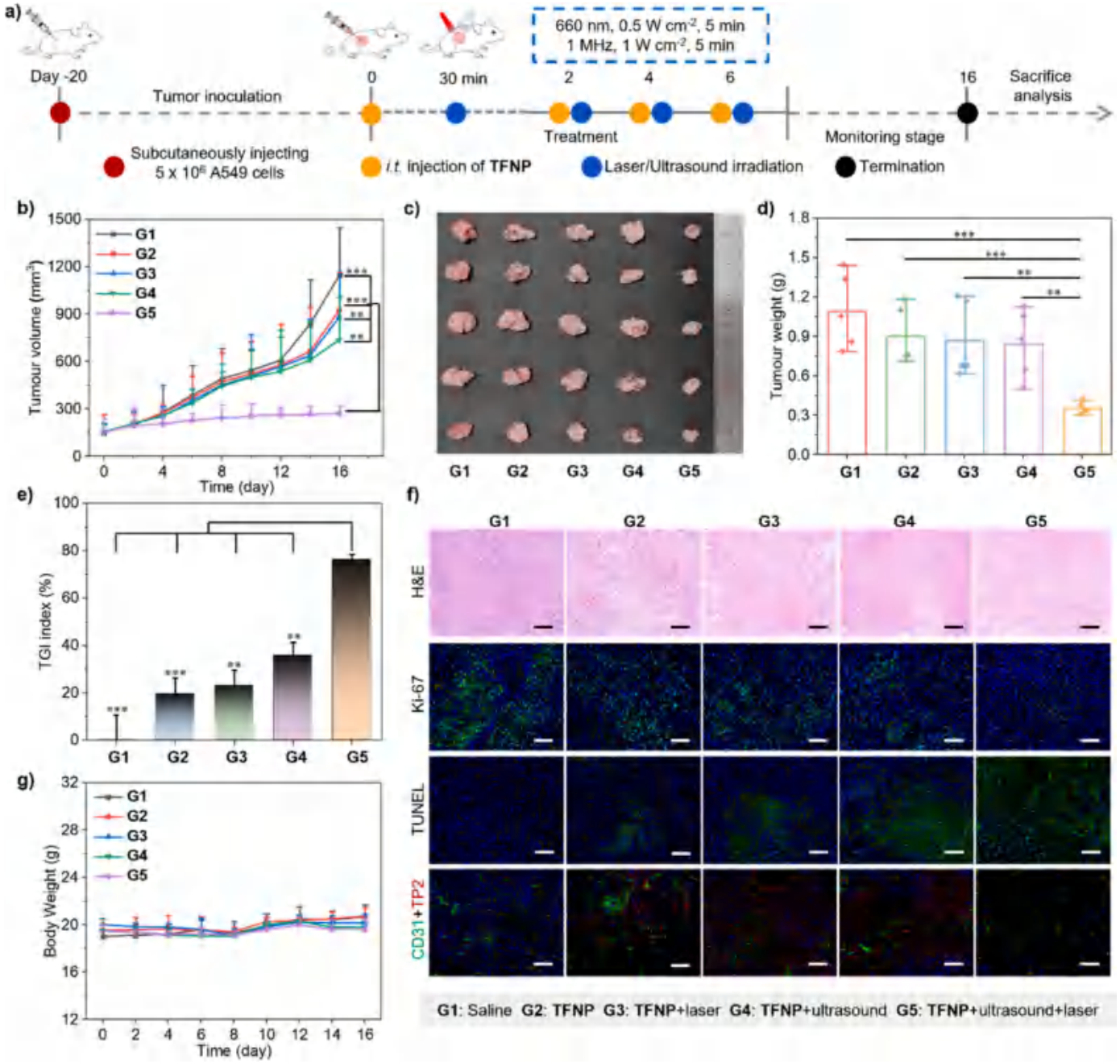

Fig. 5. Schematic of PDT-SDT schedules of intratumoral study (a). Tumor growth curves (b), images (c), weights (d), and TGI index (e) of the therapy groups. H&E, Ki-67, TUNEL and CD31+**TP2** staining of the tumor tissues (f, scale bar: 50 μm). Body weight curves of the therapy groups (g). Data are presented as mean ± SD, n = 5, * $p < 0.05$, ** $p < 0.01$, *** $p < 0.001$.

treatments were administered at 30-min intervals for three cycles, with all treatments completed within a 3-h window. The ^{19}F MRI signal exhibited only a minor reduction after these exposures (Fig. S16a), indicating that **FO1** remained largely retained within the tumor after repeated treatments. This supports the potential of **TFNP** for one-dose, multiple-imaging/therapy applications. In contrast, FLI revealed no significant signal loss with ultrasound alone, but a marked decrease after laser and combined treatments (Fig. S16b), reflecting the substantial consumption of **TP2**. The distinct imaging signatures of **FO1** and **TP2** thus enabled real-time tracking of their differential fates during therapy: **FO1** persisted within the tumor across multiple treatments within this window, whereas the integrity of **TP2** was progressively diminished by repeated laser exposure. These results underscore the value of multi-modal imaging for guiding and evaluating combination therapies in real time.

3.5. *Synergistic PDT-SDT of A549 lung cancer with **TFNP***

Since **FO1** escaped from the mice within 10 hours (Fig. 4e and f), two *in vivo* models were employed to investigate the roles of **FO1** and **TP2** in therapy: (i) *i. t.* Injection of **TFNP** with PDT and SDT 30 minutes post-injection to study the therapeutic effects of **FO1** and **TP2**, and (ii) *i. v.* injection of **TFNP** with PDT and SDT at 36 hours post-injection, at the time of maximum tumor FL intensity (Fig. 4a–d), to study the therapeutic effects of **TP2** alone.

First, the *i. t.* Study was carried out in five groups of BALB/c nude mice bearing subcutaneous A549 tumors (Fig. 5a). Once the tumors reached approximately 150 mm^3, the mice were *i. t.* Injected with either saline (**G1**) or a low dose of **TFNP** (**TP2**: 1.0 mg/kg, **G2-G5**), followed by laser/ultrasound exposure 30 minutes later. This treatment was repeated every other day for four sessions, and tumor volumes were monitored for 16 days. The greatest growth inhibition was observed in the **TFNP** + ultrasound + laser group (**G5**), whereas the **TFNP** alone (**G2**), **TFNP** + laser (**G3**), and **TFNP** + ultrasound (**G4**) groups showed minor inhibition (Fig. 5b), indicating a synergistic PDT/SDT effect. *Ex vivo* tumor photographs and weights were consistent with the tumor volume measurements (Fig. 5c and d). The tumor growth inhibition (TGI) index reached 77% for **G5**, while TGI values remained below 40% for **G2-G4** (Fig. 5e). Statistical analyses of tumor growth, tumor weight, and TGI index confirmed significant differences between **G5** and **G1-G4**.

H&E staining revealed significant tumor tissue damage in **G3-G5** compared to **G1** and **G2** (Fig. 5f). Ki-67 staining revealed the greatest suppression of tumor proliferation, and TUNEL staining showed the greatest apoptosis in **G5**. The obvious red FL of **TP2** in **G2-G4** demonstrated **TP2** retention in tumor tissue beyond the 10-h window. Notably, the green FL of CD31, a marker of endothelial cells, revealed the greatest loss of CD31-positive tumor vasculature in **G5**, suggesting substantial disruption of the tumor vasculature, which contributes to the observed

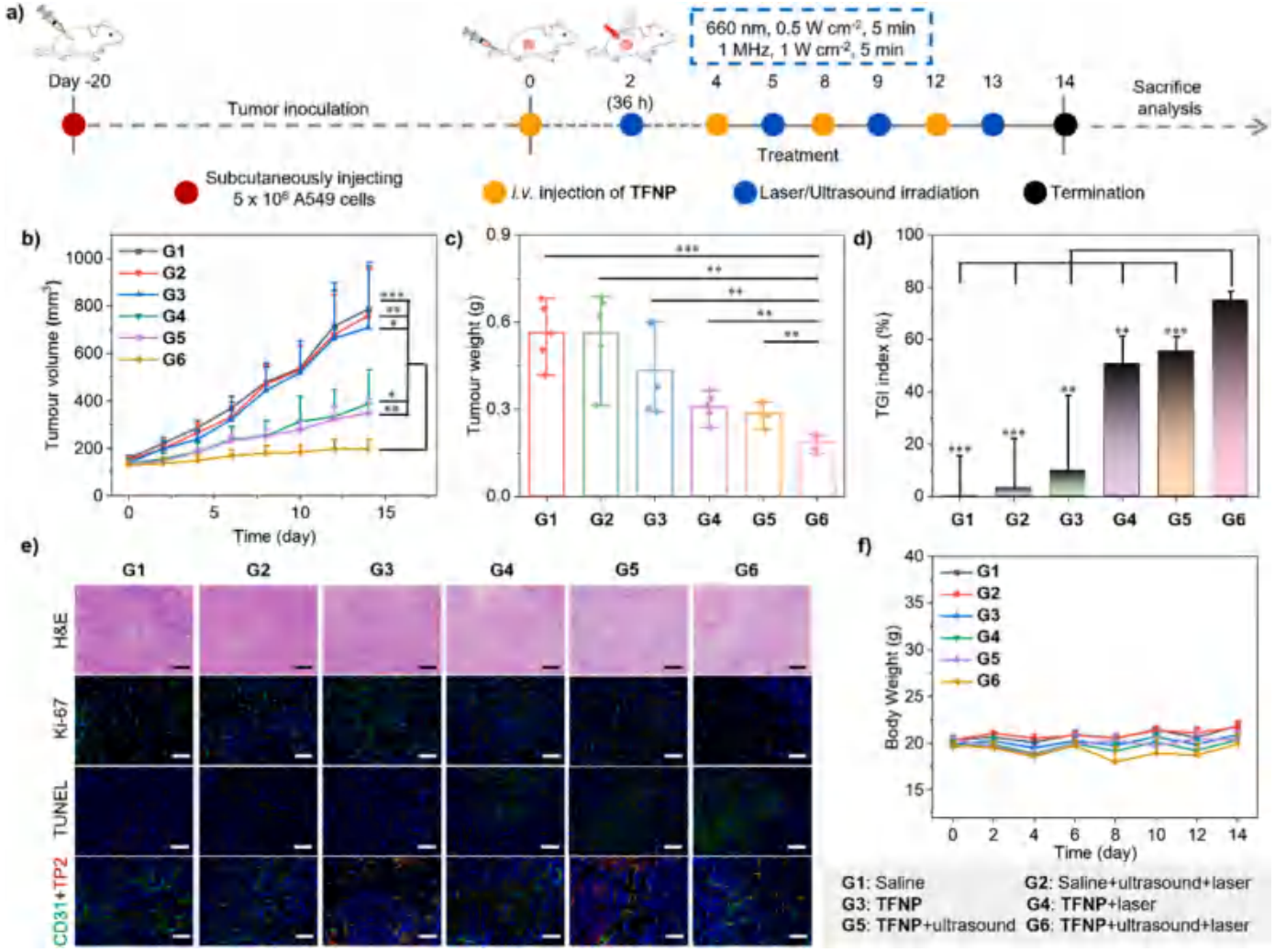

Fig. 6. Schematic of PDT-SDT schedules of intratumoral study (a). Tumor growth curves (b), weights (c), and TGI index (d) of the therapy groups. H&E, Ki-67, TUNEL and CD31+**TP2** staining of the tumor tissues (e, scale bar: 50 μm). Body weight curves of the therapy groups (f). Data are presented as mean ± SD, n = 5, $^*p < 0.05$, $^{**}p < 0.01$, $^{***}p < 0.001$.

anti-vascular effect [45]. Since cellular uptake is relatively low 30 minutes post-injection, the mechanical stress triggered by **FO1**'s phase transition upon ultrasound likely played a crucial role. This was supported by the higher apoptosis observed in **G4** than in **G3**. The low red FL of **TP2** in **G5** is likely attributable to the combined effects of **FO1** phase transition and repeated laser/ultrasound treatment, which may alter the intratumoral distribution of **TP2** and reduce its fluorescence intensity. There was no significant body-weight loss or blood chemistry abnormality (Fig. 5g and S17). H&E staining of the heart, liver, spleen, lungs, and kidneys revealed minimal off-target injury (Fig. S18). These findings demonstrate the high biosafety of **TFNP** and show that a low dose of **FO1** and **TP2** are sufficient to achieve effective PDT, SDT, and tumor vascular disruption.

Finally, the *i. v.* study was performed in six groups of BALB/c nude mice with subcutaneous A549 tumors (Fig. 6a). When the tumors reached approximately 150 mm^3, the mice were randomly assigned to six groups: saline (**G1**), saline + ultrasound + laser (**G2**), **TFNP** (**G3**), **TFNP** + laser (**G4**), **TFNP** + ultrasound (**G5**), or **TFNP** + ultrasound + laser (**G6**). **TFNP** was administered intravenously at a **TP2** dose of 5.0 mg/kg, which was selected based on preliminary biosafety evaluation. Treatments were repeated every three days for a total of four administrations. Laser and/or ultrasound irradiation was performed 36 hours post-injection (**G2** and **G4-G6**), corresponding to the time of maximal tumor FL. The **TFNP** + ultrasound + laser group (**G6**) showed the greatest tumor growth suppression (TGI 75%), followed by the **TFNP** + laser (**G4**) and **TFNP** + ultrasound (**G5**) groups, while no significant inhibition was observed in **G1-G3** (Fig. 6b–d). Histology confirmed extensive tumor damage, highest proliferation suppression, and greatest apoptosis in **G6** (Fig. 6e), with minimal body-weight loss, blood chemistry changes, or organ toxicity (Fig. 6f and S19-S20). The distinct red FL of **TP2** in groups **G3** and **G5** confirmed its targeted delivery to tumor tissue. In contrast, the absence of **TP2** fluorescence in **G4** and **G6** indicated its consumption via PDT. CD31 staining revealed no obvious tumor vascular disruption in the intravenous model.

This finding confirms that the anti-vascular effect observed in the intratumoral model is specifically triggered by the phase transition of **FO1**. These results suggest that comparable therapeutic efficacy as *i. t.* Study can be achieved through a high-dose *i. v.* injection of **TFNP**, with **TP2** acting as the active component under FLI guidance.

Taken together, these results demonstrate that the therapeutic performance of **TFNP** differs between the intratumoral and intravenous models because of their distinct delivery routes. In the intratumoral model, phase transition of **FO1** complements PDT and SDT by inducing tumor vascular disruption, whereas the intravenous model mainly demonstrates the therapeutic efficacy achievable through systemic delivery of **TFNP**. These findings further emphasize the importance of determining the theranostic windows for phase-transition nanodroplets using multimodal imaging.

4. Conclusions

In summary, "octopus-shaped" amphiphilic Janus tetraphenylporphyrins (**TP2**) and phase-transition perfluoro-*tert*-butyl methyl ether (**FO1**) were developed to self-assemble into "all-in-one" theranostic nanodroplets (**TFNP**) integrating four imaging modalities (FLI/^{19}F MRI/PAI/USI) with three therapeutic modalities (PDT/SDT/anti-vascular therapy). The synthesis of **TP2** and **FO1** is brief, efficient, and scalable. Through rational molecular design, **TP2** overcomes the poor solubility, formulation difficulty, and limited theranostic efficacy of conventional porphyrins, functioning as a versatile interfacial energy mediator and multifunctional theranostic "add-on" module. Conventional phase-transition nanodroplets have relied primarily on perfluorohexane, which exhibits suboptimal ^{19}F MRI performance due to nonequivalent fluorine environments. In contrast, **FO1** expands the available phase-transition liquids with improved physicochemical properties. Its intense singlet ^{19}F NMR peak and favorable T_2/T_1 ratio enable sensitive and quantitative "hot-spot" ^{19}F MRI in cells and tumor-bearing mice without additional labeling. **TFNP** demonstrated high biocompatibility, efficient cellular uptake with mitochondrial colocalization, and robust ROS generation *in vitro*. *In vivo* fluorescence imaging peaked at approximately 36 hours following intravenous administration, whereas intratumoral ^{19}F MRI signals persisted for less than 10 hours, defining a critical theranostic window that is often overlooked but essential for accurate interpretation of imaging-guided therapy. Guided by multimodal imaging, combined laser and ultrasound treatment achieved significant tumor growth inhibition with favorable safety profiles following both intratumoral (77% TGI) and intravenous (75% TGI) administration, highlighting the complementary therapeutic roles of **TP2** and **FO1**. Replacement of perfluorohexane with **FO1** markedly enhanced ^{19}F MRI, PAI, USI, and biocompatibility. Furthermore, low-dose **TFNP** combined with ultrasound induced vascular disruption through phase-transition-driven mechanical stress, providing an effective anti-vascular strategy. Collectively, **TFNP** represents a robust phase-transition theranostic platform and demonstrates that rational molecular and interfacial engineering can synchronize multimodal imaging with temporally optimized synergistic therapy, thereby advancing precision cancer theranostics. Future studies should focus on formulation-specific therapeutic windows for fluorocarbons with different physicochemical properties and elucidating the molecular mechanisms underlying the observed anti-vascular effect. These findings provide useful design principles for the future development and clinical translation of phase-transition theranostic nanoplatforms.

CRediT authorship contribution statement

Pei He: Data curation, Methodology, Validation, Writing – original draft. **Qiang Zhu:** Data curation, Formal analysis, Investigation, Methodology. **Ruoyun Lin:** Investigation, Methodology, Validation. **Xin Zhou:** Funding acquisition, Resources, Supervision. **Yu Li:** Conceptualization, Funding acquisition, Supervision, Writing – review & editing. **Zhong-Xing Jiang:** Conceptualization, Funding acquisition, Supervision, Writing – original draft, Writing – review & editing.

Declaration of competing interest

The authors declare that they have no known competing financial interests or personal relationships that could have appeared to influence the work reported in this paper.

Acknowledgements

This work was supported by the Strategic Priority Research Program of the Chinese Academy of Sciences (XDB0540000), the National Natural Science Foundation of China (22327901, 82441015) and the State Key Laboratory of Fluorine and Nitrogen Chemistry and Advanced Materials (2026PT0014). The authors acknowledge the use of AI-assisted language models for language editing and stylistic refinement. These tools were used solely to improve readability and linguistic quality and did not influence scientific interpretation or conclusions. All authors reviewed and approved the final manuscript.

Appendix A. Supplementary data

Supplementary data to this article can be found online at https://doi.org/10.1016/j.mtbio.2026.103463.

Data availability

Data will be made available on request.

References

[1] R.C. Fitzgerald, A.C. Antoniou, L. Fruk, N. Rosenfeld, The future of early cancer detection, Nat. Med. 28 (2022) 666–677.

[2] H. Hricak, M. Abdel-Wahab, R. Atun, M.M. Lette, D. Paez, J.A. Brink, L. Donoso-Bach, G. Frija, M. Hierath, O. Holmberg, P.-L. Khong, J.S. Lewis, G. McGinty, W.J. G. Oyen, L.N. Shulman, Z.J. Ward, A.M. Scott, Medical imaging and nuclear medicine: a lancet oncology commission, Lancet Oncol. 22 (2021) e136–e172.

[3] R. Jiang, J. Dai, X. Dong, Q. Wang, Z. Meng, J. Guo, Y. Yu, S. Wang, F. Xia, Z. Zhao, Improving image-guided surgical and immunological tumor treatment efficacy by photothermal and photodynamic therapies based on a multifunctional NIR AIEgen, Adv. Mater. 33 (2021) 2101158.

[4] D. Zhuang, H. Zhang, G. Hu, B. Guo, Recent development of contrast agents for magnetic resonance and multimodal imaging of glioblastoma, J. Nanobiotechnol. 20 (2022) 284.

[5] L. Zhang, G. Oudeng, F. Wen, G. Liao, Recent advances in near-infrared-II hollow nanoplatforms for photothermal-based cancer treatment, Biomater. Res. 26 (2022) 61.

[6] K. Wilson, K. Homan, S. Emelianov, Biomedical photoacoustics beyond thermal expansion using triggered nanodroplet vaporization for contrast-enhanced imaging, Nat. Commun. 3 (2012) 618.

[7] O. Shpak, M. Verweij, H.J. Vos, N. de Jong, D. Lohse, M. Versluis, Acoustic droplet vaporization is initiated by superharmonic focusing, Proc. Natl. Acad. Sci. USA 111 (2014) 1697–1702.

[8] D.G. Ramirez, E. Abenojar, C. Hernandez, D.S. Lorberbaum, L.A. Papazian, S. Passman, V. Pham, A.A. Exner, R.K. Benninger, Contrast-enhanced ultrasound with sub-micron sized contrast agents detects insulitis in mouse models of type1 diabetes, Nat. Commun. 11 (2020) 2238.

[9] Q. Zhang, Y. Yang, H. Xue, H. Zhang, Z. Yuan, Y. Shen, X. Guo, Z. Fan, X. Wu, D. Zhang, Intensified and controllable vaporization of phase-changeable nanodroplets induced by simultaneous exposure of laser and ultrasound, Ultrason. Sonochem. 94 (2023) 106312.

[10] Y.-J. Ho, C.-K. Yeh, Concurrent anti-vascular therapy and chemotherapy in solid tumors using drug-loaded acoustic nanodroplet vaporization, Acta Biomater. 49 (2017) 472–485.

[11] R. Gao, E. Wang, V. Pineiro, L. Chudal, J. Santelli, C. Endsley, A. Woodward, C. de Gracia Lux, J. Lux, R.F. Mattrey, Perfluorohexane emulsions induce macrophage-stimulating effects through iNOS expression, ACS Appl. Bio Mater. 8 (2025) 4046–4054.

[12] K. Chen, J. He, A. Zhou, J. Zhu, S. Sheng, Z. Fu, X. Ning, Ultrasound-activated sonophage synergizes sonodynamic therapy and saltoptosis for solid tumor eradication, Adv. Mater. 38 (2026) e08245.

[13] S.M. Thompson, K.R. Gorny, E.M.K. Koepsel, B.T. Welch, L. Mynderse, A. Lu, C. P. Favazza, J.P. Felmlee, D.A. Woodrum, Body interventional MRI for diagnostic and interventional radiologists: current practice and future prospects, Radiographics 41 (2021) 1785–1801.

[14] F. Calivà, N.K. Namiri, M. Dubreuil, V. Pedoia, E. Ozhinsky, S. Majumdar, Studying osteoarthritis with artificial intelligence applied to magnetic resonance imaging, Nat. Rev. Rheumatol. 18 (2022) 112–121.

[15] R. Zhang, K. Wang, W. Xiao, D. Wu, Z. Cao, Self-immolative fluorinated nanotheranostics amplifying ^{19}F MRI signals for tumor-specific imaging and photodynamic therapy, J. Contr. Release 387 (2025) 114217.

[16] F. Zeng, Z. Fan, S. Li, L. Li, T. Sun, Y. Qiu, L. Nie, G. Huang, Tumor microenvironment activated photoacoustic-fluorescence bimodal nanoprobe for precise chemo-immunotherapy and immune response tracing of glioblastoma, ACS Nano 17 (2023) 19753–19766.

[17] B. Chu, Z. Chen, H. Shi, X. Wu, H. Wang, F. Dong, Y. He, Fluorescence, ultrasonic and photoacoustic imaging for analysis and diagnosis of diseases, Chem. Commun. 59 (2023) 2399–2412.

[18] R. Zhou, H. Sha, S. Fu, G. Liu, J. Wei, C. Wang, S. Hou, G. Lu, Hyperspectral fluorescence imaging with a new polarity-ultrasensitive fluorescent probe, Adv. Sci. 12 (2025) e08792.

[19] D. Wang, C. Xing, Y. Liang, C. Wang, P. Zhao, X. Liang, Q. Li, L. Yuan, Ultrasound imaging of tumor vascular CD93 with MMRN2 modified microbubbles for immune microenvironment prediction, Adv. Mater. 36 (2024) 2310421.

[20] Y. Zhang, S. Bo, T. Feng, X. Qin, Y. Wan, S. Jiang, C. Li, J. Lin, T. Wang, X. Zhou, Z.-X. Jiang, P. Huang, A versatile theranostic nanoemulsion for architecture-dependent multimodal imaging and dually augmented photodynamic therapy, Adv. Mater. 31 (2019) 1806444.

[21] T.C. Pham, V.-N. Nguyen, Y. Choi, S. Lee, J. Yoon, Recent strategies to develop innovative photosensitizers for enhanced photodynamic therapy, Chem. Rev. 121 (2021) 13454–13619.

[22] H. Wang, T. Qin, W. Wang, X. Zhou, F. Lin, G. Liang, Z. Yang, Z. Chi, B.Z. Tang, Selenium-containing type-I organic photosensitizers with dual reactive oxygen species of superoxide and hydroxyl radicals as switch-hitter for photodynamic therapy, Adv. Sci. 10 (2023) 2301902.

[23] M. Won, S. Koo, H. Li, J.L. Sessler, J.Y. Lee, A. Sharma, J.S. Kim, An ethacrynic acid-brominated BODIPY photosensitizer (EA-BPS) construct enhances the lethality of reactive oxygen species in hypoxic tumor-targeted photodynamic therapy, Angew. Chem., Int. Ed. 60 (2021) 3196–3204.

[24] X. Wang, X. Zhong, F. Gong, Y. Chao, L. Cheng, Newly developed strategies for improving sonodynamic therapy, Mater. Horiz. 7 (2020) 2028–2046.

[25] J. An, Y.-G. Hu, K. Cheng, C. Li, X.-L. Hou, G.-L. Wang, X.-S. Zhang, B. Liu, Y.-D. Zhao, M.-Z. Zhang, ROS-augmented and tumor-microenvironment responsive biodegradable nanoplatform for enhancing chemo-sonodynamic therapy, Biomaterials 234 (2020) 119761.

[26] P. Wen, W. Xie, D. Zhong, Z. Li, Y. Li, Emerging applications of photodynamic and sonodynamic therapies in orthopedic disorders: mechanisms, challenges, and future directions, Adv. Healthcare Mater. 14 (2025) e02565.

[27] R. Qu, X. Jiang, X. Zhen, Light/X-ray/ultrasound activated delayed photon emission of organic molecular probes for optical imaging: mechanisms, design strategies, and biomedical applications, Chem. Soc. Rev. 53 (2024) 10970–11003.

[28] Z. Wang, B. Zhu, W. Nie, L. Zhang, N. Xiao, Q. Zhang, Z. Wu, C. Shi, W. Zhu, Q. Liu, D. Zhu, M.R. Bryce, L. Ren, B.Z. Tang, Endogenous near-infrared chemiluminescence: imaging-guided non-invasive thrombolysis and anti-inflammation based on a heteronuclear transition metal complex, Adv. Sci. 12 (2025) 2501257.

[29] G.-Q. Jin, C.V. Chau, J.F. Arambula, S. Gao, J.L. Sessler, J.-L. Zhang, Lanthanide porphyrinoids as molecular theranostics, Chem. Soc. Rev. 51 (2022) 6177–6209.

[30] M. Ishikawa, S. Tomoshige, S. Sato, Challenges of aufheben to promote druglikeness: chemical modification strategies to improve aqueous solubility and permeability, J. Med. Chem. 68 (2025) 20859–20902.

[31] W. Zhang, H. Metzger, S. Vlatakis, A. Claxton, M.A. Carbajal, L.F. Fung, J. Mason, K.A. Chan, A.N. Pouliopoulos, R.A. Fleck, Characterising the chemical and physical properties of phase-change nanodroplets, Ultrason. Sonochem. 97 (2023) 106445.

[32] Z. Mo, Q. Li, K. Zhao, Q. Xu, H. Hu, X. Chen, Y. Luo, B. Chi, L. Liu, X. Fang, G. Liao, Z. Xu, J. Wang, S. Yang, A nanoarchitectonic approach enables triple modal synergistic therapies to enhance antitumor effects, J. Contr. Release 169 (2013) 141–149.

[33] H. Xie, W. Li, H. Liu, Y. Chen, M. Ma, Y. Wang, Y. Luo, D. Song, Q. Hou, W. Lu, Y. Bai, B. Li, J. Ma, C. Huang, T. Yang, Z. Liu, X. Zhao, P. Ding, Erythrocyte membrane-coated invisible acoustic-sensitive nanoparticle for inducing tumor thrombotic infarction by precisely damaging tumor vascular endothelium, Small 18 (2022) 2201933.

[34] Q. Chen, H. Yu, L. Li, H. Zhang, M. Tan, W. Liu, M. Zheng, Y. Hu, L. Cheng, Y. Chen, An imaging-guided self-amplifying photo-immunotherapeutic nanoparticle for STING pathway activation and enhanced cancer therapy, J. Nanobiotechnol. 23 (2025) 459.

[35] H. Zhang, Q. Yu, Y. Li, Z. Yang, X. Zhou, S. Chen, Z.-X. Jiang, Fluorinated cryptophane-A and porphyrin-based theranostics for multimodal imaging-guided photodynamic therapy, Chem. Commun. 56 (2020) 3617–3620.

[36] G. Linden, L. Zhang, F. Pieck, U. Linne, D. Kosenkov, R. Tonner, O. Vázquez, Conditional singlet oxygen generation through a bioorthogonal DNA-targeted tetrazine reaction, Angew. Chem., Int. Ed. 58 (2019) 12868–12873.

[37] Y. Zheng, L. Zhu, C. Ke, Y. Li, Z. Zhou, M. Jiang, F. Wang, P. He, X. Zhou, Z.-X. Jiang, Fluorinated macromolecular amphiphiles as prototypic molecular drones, Proc. Natl. Acad. Sci. U. S. A. 121 (2024) e2405877121.

[38] M. Zare, K.S. Mikkonen, Phase change materials for life science applications, Adv. Funct. Mater. 33 (2023) 2213455.

[39] Y. Ji, J. Zheng, Z. Geng, X. Wang, Y. Hou, J. Tian, J. Hu, Y. Zhang, L. Zhang, Fluorocarbon nanodroplets: their formation and stability in complex solution systems, Langmuir 40 (2024) 9108–9119.

[40] E. Lepeltier, C. Bourgaux, P. Couvreur, Nanoprecipitation and the "ouzo effect": application to drug delivery devices, Adv. Drug Deliv. Rev. 71 (2014) 86–97.

[41] M.A. Vratsanos, W. Xue, N.D. Rosenmann, L.D. Zarzar, N.C. Gianneschi, Ouzo effect examined at the nanoscale via direct observation of droplet nucleation and morphology, ACS Cent. Sci. 9 (2023) 457–465.

[42] D.S. Li, S. Schneewind, M. Bruce, Z. Khaing, M. O'Donnell, L. Pozzo, Spontaneous nucleation of stable perfluorocarbon emulsions for ultrasound contrast agents, Nano Lett. 19 (2019) 173–181.

[43] H. Moon, G.-J. Jeong, T.S. Reddy, D.H. Yang, M.-S. Choi, Porphyrin-based fluorescent probes for imaging mitochondria in living cells, Dyes Pigments 231 (2024) 112369.

[44] Q. Chen, H. Xiao, L. Hu, Y. Huang, Z. Cao, X. Shuai, Z. Su, ^{19}F MRI/CEUS dual imaging-guided sonodynamic therapy enhances immune checkpoint blockade in triple-negative breast cancer, Adv. Sci. 11 (2024) 2401182.

[45] P. Liang, B. Ballou, X. Lv, W. Si, M.P. Bruchez, W. Huang, X. Dong, Monotherapy and combination therapy using anti-angiogenic nanoagents to fight cancer, Adv. Mater. 33 (2021) 2005155.